Research Article | Vol. 13, No. 2 / 1 Feb 2023 / Optical Materials Express 357
Optical Materials EXPRESS

Crystallization of high gyrotropy garnets with decreasing thermal processing budgets as analyzed by electron backscatter diffraction

KARTHIK SRINIVASAN,[1,2,*] NICHOLAS C. A. SEATON,[3] RUOMING PENG,[4] MO LI,[4] AND BETHANIE J. H. STADLER[1,5]

[1]Department of Electrical and Computer Engineering, University of Minnesota, 200 Union St SE, Minneapolis, MN 55455, USA
[2]Currently with the Department of Electrical and Computer Engineering, Cornell University, 116 Hoy Road, 114 Phillips Hall, Ithaca, NY 14853, USA
[3]College of Science and Engineering Characterization Facility, University of Minnesota, Shepherd Laboratory, 100 Union St SE, Minneapolis, MN 55455, USA
[4]Department of Electrical and Computer Engineering, University of Washington, Seattle, WA 98195, USA
[5]stadler@umn.edu
[*]srini162@umn.edu

Abstract: Rare-earth iron garnets with large magnetic gyrotropy, made with reduced thermal budgets, are ideal magneto-optical materials for integrated isolators. However, reduced thermal budgets impact Faraday rotation by limiting crystallization, and characterization of crystallinity is limited by resolution or scannable area. Here, electron backscatter diffraction (EBSD) is used to measure crystallinity in cerium substituted yttrium- and terbium-iron garnets (CeYIG and CeTbIG) grown on planar Si, crystallized using one-step rapid thermal processes, leading to large Faraday rotations > −3500 °/cm at 1550 nm. Varying degrees of crystallinity are observed in planar Si and patterned Si waveguides, and specific dependences of crystallite size are attributed to the nucleation/growth processes of the garnets and the lateral dimensions of the waveguide. On the other hand, a low thermal budget alternative–exfoliated CeTbIG nanosheets–are fully crystalline and maintain high Faraday rotations of −3200 °/cm on par with monolithically integrated thin film garnets.

1. Introduction

Optical isolators are passive devices that block reflections from destabilizing a laser [1–3]. Successful isolation has been achieved using magneto-optical garnets that have large gyrotropy in the presence of a small magnetic bias [4,5] and even no external magnetic bias [6,7]. Faraday rotation is a manifestation of gyrotropy that causes the polarization state of light to rotate non-reciprocally, such that reflections are orthogonal to the input and they can be filtered before reaching the laser. Faraday rotation is linear with optical path, so high gyrotropy materials can provide isolation with small footprints. Commercially, optical isolators comprise of a bulk piece of magneto-optical garnet and two orthogonal polarizing filters placed in the light path with an assembly of mirrors and lenses. In these isolators, each component is placed in their respective position using high-throughput automated pick and place techniques. However, in photonic integrated circuits (PIC), where the laser is bonded to the chip, it would be beneficial to have isolators that are on the same waveguide platform. Integrated waveguide isolators require a garnet cladding to utilize one of two phenomena for optical isolation: non-reciprocal mode conversion (NRMC) or the non-reciprocal phase shift (NRPS) [8–10]. As the name suggests, NRMC devices convert the propagating mode between fundamental transverse electric (TE) and transverse magnetic (TM) modes (the waveguide equivalent to Faraday rotation). NRPS devices

#476482 https://doi.org/10.1364/OME.476482
Journal © 2023 Received 27 Sep 2022; revised 24 Oct 2022; accepted 10 Nov 2022; published 3 Jan 2023

Optical Materials EXPRESS

create a phase difference in interferometers or resonators, such that there is constructive (forward) or destructive (backward) interference [1,11,12].

Isolation, using either NRMC or NRPS, relies on the successful integration of waveguides with garnets for coupling with their magneto-optical properties. Garnets are monolithically integrated using pulsed laser deposition (PLD) or sputter deposition, or they are heterogeneously integrated using wafer bonding to the device wafer [13–15]. Monolithically integrated garnets are typically annealed *in-situ* during or after deposition, or *ex-situ* in a rapid thermal annealer (RTA) to obtain the desired phase. Some substituted garnets (such as CeYIG or BiYIG) with better Faraday rotations require a seedlayer to obtain desired phase crystallinity, which can introduce additional lithographic alignment and annealing steps [16–18]. On the other hand, with heterogenous integration the device wafer is not exposed to high temperatures at all because the garnet is grown on a separate substrate and processed before being bonded to the wafer [12]. Wafer bonding of single crystal garnets grown on single crystalcrystal gadolinium gallium substrates only requires 200°C and a few MPa of pressure. However, the millimeter dimensions of the garnet die and the thick substrates can limit scalability of the device density. Heterogenous integration of exfoliated garnet nanosheets is a scalable alternative that conforms to the dimensions of the waveguides [19].

Annealing at a high temperature provides the activation energy for the nucleation and growth of crystallites in the desired garnet phase, and crystallinity determines the magneto-optical properties (viz. Faraday rotation and losses) of the garnets. Large Faraday rotations in the range of −1800 to −3800 °/cm have been shown in substituted yttrium iron garnets; YIG (CeYIG, BiYIG) and substituted terbium iron garnets; TbIG (CeTbIG and BiTbIG), and they have usually required annealing temperatures > 800 °C [7,17,18,20,21]. But, such thermal processes are difficult to integrate with Si as the back end of the line CMOS process is limited to temperatures below the metal/Si eutectic points, which lies at 577 °C for Al-Si to 802 °C for Cu-Si [22,23]. Therefore, the tradeoff for successful garnet integration is either integration prior to CMOS or keeping the thermal budgets low while still achieving a high degree of crystallization for better Faraday rotations.

Quantifying crystallinity will help in finding pathways for reducing the thermal budgets. However, the most popular methods of measuring crystallization are X-ray diffraction (XRD), which doesn't have high enough resolution, or high-resolution transmission electron microscope (HRTEM), which only measures small areas and involves tedious sample prep (often destructive cross sections) [24–26].

Here, electron backscatter diffraction (EBSD) is used to measure the crystallinity over large areas with single grain resolution on three different types of thin film garnets with decreasing thermal budgets. The garnets characterized in this paper and their maximum thermal budget for 100% crystallinity are: (i) YIG/CeYIG thin films annealed in dual-temperature single-step RTA process with a maximum temperature of 950 °C, (ii) CeTbIG thin films annealed in a one-temperature single-step RTA process with a maximum temperature of 900 °C and (iii) exfoliated CeTbIG nanosheets for transfer integration with device wafers which will therefore experience no impact to their thermal budget. Specifically, the differences in crystallinity are highlighted for garnet on planar silicon substrates, garnet on patterned silicon waveguides, and exfoliated garnet (no substrate). It is also observed that the annealing processes required to obtain fully crystalline garnets vary between planar and patterned substrates. Large Faraday rotations are achieved in CeYIG and CeTbIG using a single-step rapid thermal process and in exfoliated CeTbIG. Characterization of crystallinity at single crystallite resolution is also shown in exfoliated nanosheets, which was otherwise deemed challenging due to lack of a substrate and the nonplanar surface of the transfer adhesive. The garnets and the processes discussed in this paper are instrumental to the realization of fully integrated optical isolators and reducing the thermal budget that has otherwise prevented their integration using standard foundry processes.

Optical Materials EXPRESS

2. Results and discussion

2.1. Ce-substituted yttrium iron garnets

The first set of garnet thin films that are quantified using EBSD are cerium substituted yttrium iron garnets (CeYIG) that are reactively sputter deposited on planar Si substrates and patterned Si waveguides. Elemental composition analysis using energy dispersive X-ray spectroscopy (EDS) reveals a near-ideal stoichiometry of $Ce_{0.9}Y_{2.4}Fe_{4.7}O_{12}$. CeYIG has often required either a bottom or top seedlayer of an undoped YIG thin film to crystallize in the desired phase upon rapid thermal annealing. Typically, undoped YIG is first deposited on the substrate, annealed at a high temperature > 900 °C, which is followed by deposition and annealing of the substituted CeYIG thin film. EBSD in Fig. 1(a) shows planar Si/YIG (20 nm)/CeYIG (140 nm) thin films after two annealing steps each at 900 °C for 3 min in oxygen, once for the seed layer and later for the substituted layer. These EBSD images lack the characteristic "stained-glass" like orientation contrast that is typical of polycrystalline materials. However, the X-ray diffraction spectra shown in the inset gives an appearance of a fully crystalline thin film. The discrepancy between the EBSD and XRD measurements suggest that the garnets are present but only in the form of nanocrystallites, which is evident from the lack of diffraction band contrast in the EBSD image. Even though the garnet is in a nanocrystalline phase, it still has useful magneto-optical properties because large Faraday rotations are observed in YIG/CeYIG that follow the two-step annealing process.

A better tradeoff between thermal budget and crystallization was sought by using an intermediary low-temperature anneal (at 500 °C) prior to the high-temperature anneal (at 800 °C – 900 °C) and through bottom and top seed layers to promote simultaneous nucleation events from two interfaces. Thin films of YIG (20 nm)/CeYIG (75 nm)/YIG (75 nm) annealed at 500 °C for 30 s followed by 900 °C for 3 mins (one time anneal for the combined seed layers and substituted layer) showed crystalline diffraction spectra (as shown in Fig. S1 in the Supplement 1) but had poor Faraday rotations. Comparison of Faraday rotation with the annealing process does not indicate a significant improvement to gyrotropy from the intermediary annealing step (Fig. 5). Furthermore, quantification of CeYIG crystallization using EBSD from garnets with a top seed layer is challenging owing to undifferentiated band contrasts from the YIG and CeYIG layers. That is, a crystalline YIG phase from the top seedlayer and a nanocrystalline CeYIG phase cannot be decoupled in an EBSD map in inverse pole figure (IPF) colors that shows the different spatial orientations. While Gage et al. showed that a two-step annealing process overcomes the nanocrystalline phase and produces a fully crystalline phase in YIG thin films, it is likely that the substituted garnets require a higher temperature for nucleation and growth [27].

Therefore, a higher initial temperature was chosen to promote grain nucleation, which was followed by a longer anneal at the reduced temperature for grain growth without the formation of detrimental secondary phases. Thin films of YIG (20 nm)/CeYIG (140 nm) on Si annealed at a high temperature of 950 °C for 90 s followed by reduced temperature of 900 °C for 4 min in oxygen produce fully crystalline films with distinct randomly oriented crystallites ("stained-glass" like contrast) as shown in Fig. 1(b). The YIG seedlayer was not annealed prior to CeYIG deposition, and both YIG/CeYIG are annealed in a single annealing process.

Interestingly, when the same annealing process is applied to YIG/CeYIG claddings on silicon waveguides, whose cross-section is shown in Fig. 1(c), the crystallinity has a dependence on the width of the waveguide. Figure 1(d) shows that in waveguides with a width of 1 µm, the crystallites of CeYIG are confined laterally by the width of the waveguide. However, in waveguides with a width of 2 µm (Fig. 1(e)), nucleation of multiple crystallites along the width is observed. This trend was continued by a visible presence of several crystallites along the lateral dimension in waveguides with a width of 4 µm in Fig. 1(f). ImageJ analysis further showed that crystallinity improves from 25% to 72% upon increasing the width of the waveguide, indicating that the surface

Optical Materials EXPRESS

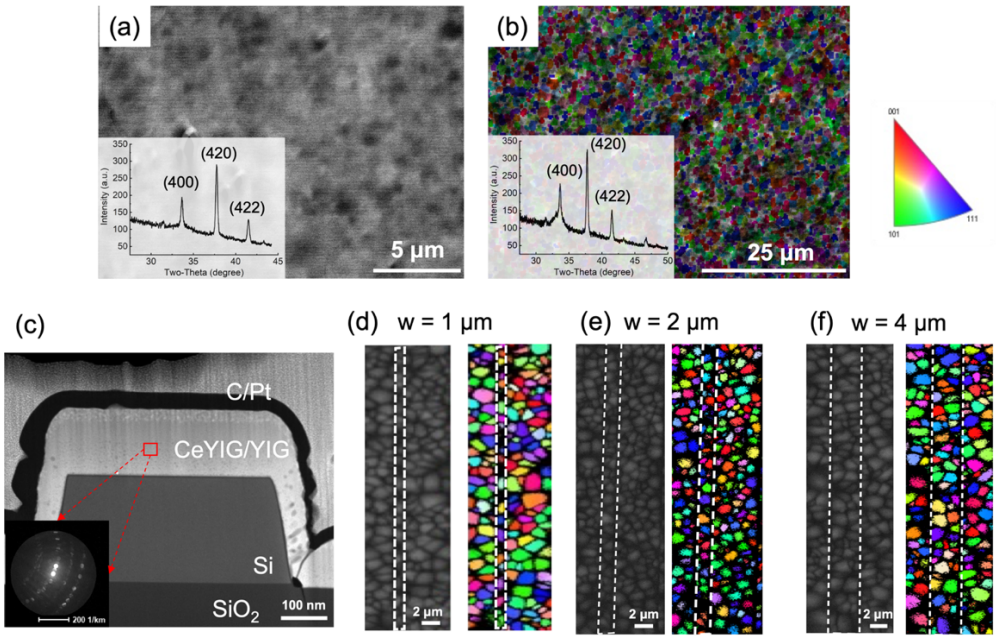

Fig. 1. Electron backscatter diffraction (EBSD) analysis of YIG/CeYIG (140 nm) thin films. (a) Forescatter detector (FSD) image of Si/YIG/CeYIG annealed at 900 °C for 3 min shows a low contrast nanocrystalline phase and corresponding XRD spectra in the inset. (b) Overlay of EBSD map in inverse pole figure (IPF) colors on the forescatter image of Si/YIG/CeYIG annealed at 950 °C for 90 s followed by 900 °C for 4 mins shows fully crystalline garnet and corresponding XRD spectra in the inset. The IPF is the triangle that shows spatial orientations in crystallographic space. (c) Cross-section scanning transmission electron microscope (STEM) image of Si waveguides patterned into Si-on-insulator (SOI) wafers with YIG/CeYIG cladding and C/Pt capping layers. (inset) Select area electron diffraction pattern of polycrystalline CeYIG. (d)-(f) Band contrast images (left) and IPF colored EBSD maps (right) of YIG/CeYIG claddings on Si waveguides of varying widths (1 µm, 2 µm and 4 µm) patterned into SOI wafers. In this top view, the waveguides are differentiated from the oxide by the white dashed lines.

area available is critical in promoting multiple nucleation and growth events for YIG/CeYIG films. While the width of the waveguide determines the number of crystallites, uniform crystallinity is achieved through the thickness of the cladding from the annealing processes used here as shown in the cross-section select area electron diffraction from a scanning transmission electron microscope (inset in Fig. 1(c) and Fig. S2).

2.2. Ce-substituted terbium iron garnets

The discussion thus far has been on CeYIG which requires a seedlayer, and in some cases, an additional annealing step to crystallize the seedlayer before depositing the substituted garnet. Alternatively, garnets based on terbium and its substituted variants such as BiTbIG and CeTbIG do not require seedlayers to form the desired phase on silicon substrates and Faraday rotations as large as −3200 °/cm have been obtained [21,28]. Previous reports have shown that isolators designed using BiTbIG and CeTbIG provide near ideal isolation ratio of 30 dB in quasi one-dimensional NRMC device footprints of 5-7 mm [6,7]. Importantly, these devices did not require an external magnetic field, but rather the shape anisotropy of the garnet layers was enough to hold the magnetization along the preferred direction in a remnant state. However, upon annealing at

Optical Materials EXPRESS

900 °C for 3 min, $Ce_{0.8}Tb_{2.2}Fe_{4.7}O_{12}$ (140 nm) thin films with near-ideal stoichiometry are only quasi-crystalline on both planar Si/SiO_2 and patterned Si waveguides on silicon-on-insulator (SOI) substrates, as shown in Fig. 2(a-b). Note that these films appear to be in the desired polycrystalline phase from XRD measurements (inset in Fig. 2(a)). Even after reannealing at 950 °C for 3 min, the corresponding IPF colored EBSD maps show no apparent change in crystallinity, but the individual crystallites are larger than before, as seen in the oxide regions adjacent to the waveguide in Fig. 2(c). An analysis of the IPF colored EBSD map on planar Si and the patterned Si waveguide using ImageJ shows that far fewer crystallites nucleate and grow on the waveguide compared to the planar substrate for the same thermal processing conditions.

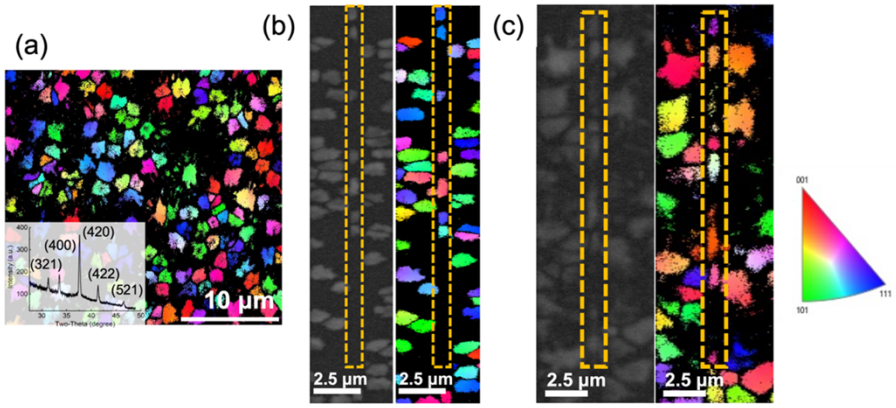

Fig. 2. EBSD crystallinity analysis of Si/CeTbIG (140 nm) thin films. (a) IPF colored EBSD maps of CeTbIG thin film on planar Si substrate annealed at 900 °C for 3 mins shows partially crystalline films and corresponding XRD spectra in the inset. (b) CeTbIG cladding on Si waveguide annealed at 900 °C for 3 min. (c) CeTbIG cladding on Si waveguide reannealed at 950 °C for 3 min. The waveguides are marked by yellow dashed lines.

Fully crystalline CeTbIG thin films on planar Si and patterned Si waveguides are obtained by increasing the annealing time to 5 minutes from the previously set 3 minutes as shown in Fig. 3(a-b). The crystallinity on planar Si improves from 40% to over 95% after the longer anneal. Unlike CeYIG, which required a higher temperature to initiate nucleation, CeTbIG crystallites nucleated at 900 °C and only required a longer anneal time for the crystallite growth. Moreover, in contrast to CeYIG, whose crystallite size was less than 1 μm, the CeTbIG crystallites are larger (about 2-4 μm) and a single crystallite tends to span the entire width of the waveguide as seen in Fig. 3(c-e). The crystallinity of the garnet on the waveguide does not change with the width as in the case of CeYIG. This is because the nucleation sites of most CeTbIG crystallites lie on the neighboring oxide region of the SOI wafer and the growth process extends the crystallite on to the waveguides. Such a behavior is not observed in CeYIG, where each crystallite appears to have a nucleation site on the waveguide itself. It must be noted that both CeYIG and CeTbIG claddings compared here are of the same thickness (140 nm) and extend over the neighboring oxide region without discontinuities.

While higher temperatures or longer annealing processes results in favorable crystallinity in garnets, as seen in Fig. 1 through 3, incorporating such a process in a photonic foundry could be challenging if CMOS devices are needed on the same wafer. Exfoliation of garnet thin films from planar substrates into large nanosheets through a diffusion-driven exfoliation process is a new low thermal budget pathway of integrating them with photonic platforms [19]. Exfoliation is possible when CeTbIG thin films are annealed at 950 °C for 30 s followed by 900 °C for 5 min such that the diffusion of cations away from the substrate interface creates an exfoliation gap. Mechanical

Optical Materials EXPRESS

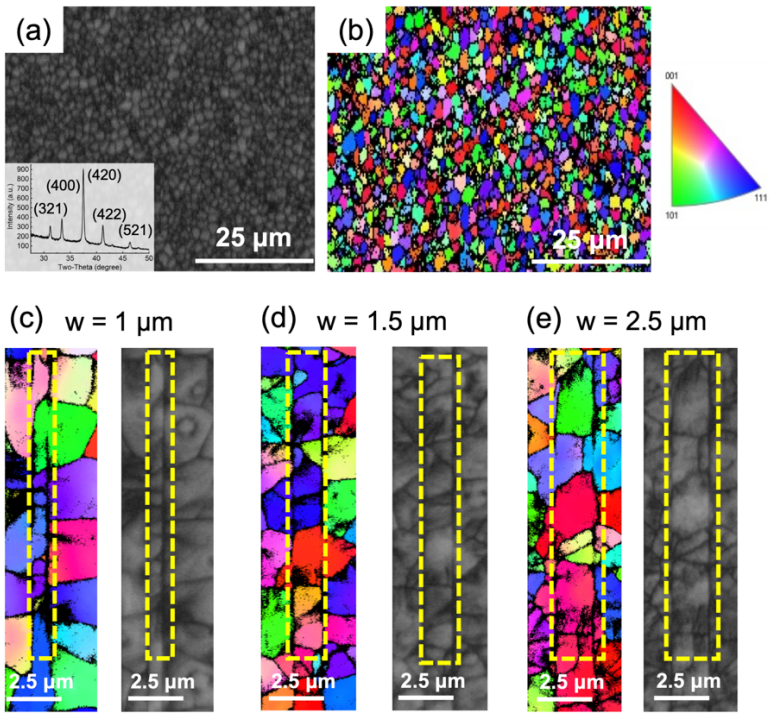

Fig. 3. EBSD crystallinity analysis of CeTbIG (140 nm) thin films annealed for longer times (5 min) at 900 °C. (a) Band contrast image showing the diffraction contrast of crystalline thin films on planar Si and corresponding XRD spectra in the inset. (b) IPF colored EBSD maps shows a fully crystalline thin film on planar Si with randomly oriented crystallites. (c)-(e) Fully crystalline CeTbIG cladding on patterned Si waveguides on SOI of varying widths from 1–2.5 μm. The waveguides are differentiated from the underlying oxide by yellow dashed lines.

exfoliation from the handle wafer results in nanosheets of garnets that can be further transfer printed onto device wafers. Such a process allows the device wafer to circumvent detrimental high temperature annealing while still benefitting from the desirable magneto-optical properties of garnets. Like garnets on waveguides, exfoliated nanosheets are difficult to characterize using XRD, and instead benefit from EBSD. In this paper, we show successful EBSD imaging of CeTbIG nanosheets (Fig. 4), including the EBSD band contrast image and IPF colored EBSD maps, which indicate that the exfoliated nanosheet is fully crystalline in the desired garnet phase. Here, the garnet is crystallized on a planar Si substrate prior to exfoliation, which means that crystallization dynamics are not limited by the available surface area between the film and the substrate. However, if garnets are transfer printed from a patterned handle wafer on to the device wafer with a feature-to-feature alignment, the mutual dependencies between waveguide width, thermal processes and crystallinity must be considered. Furthermore, if nucleation sites of some garnets lie on the oxide regions adjacent to the waveguide, deep trenches around waveguides might be needed to isolate the cladding for nucleation to proceed on Si as shown earlier with CeYIG.

2.3. *Magneto-optical properties*

Magneto-optical measurements in Fig. 5 show the Faraday rotation measured in all the garnet films from this work and some reference measurements from literature. In CeYIG thin films,

Optical Materials EXPRESS

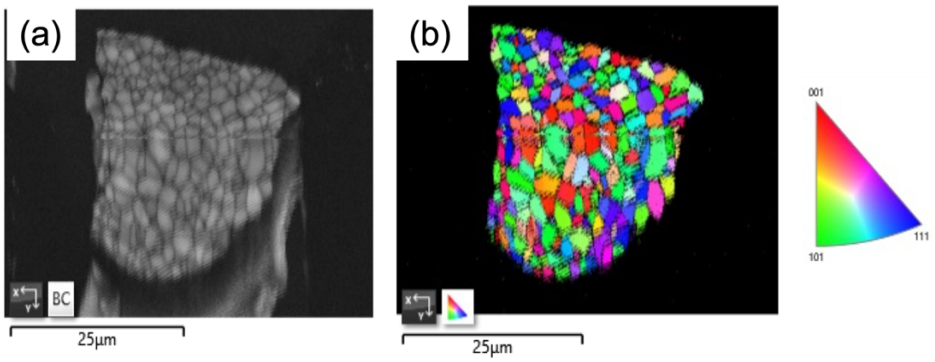

Fig. 4. EBSD crystallinity analysis of exfoliated CeTbIG (126 nm) nanosheet. (a) Band contrast image of exfoliated nanosheet shows uniformly spread crystallites of the desired phase. (b) IPF colored EBSD map shows crystallites indicative of the polycrystalline nature.

Faraday rotation varies with both the seedlayer placement and the annealing process. For instance, Si/YIG/CeYIG with just the bottom seedlayers have better Faraday rotations (> -3000 °/cm) than the Si/YIG/CeYIG/YIG thin films with both bottom and top seedlayers (< -2000 °/cm). Specifically, Si/YIG/CeYIG films annealed using the 950 °C and 900 °C process (single annealing step) has a Faraday rotation of −3800 °/cm compared to −3400 °/cm for the Si/YIG/CeYIG films annealed at 900 °C (two annealing steps for seedlayer and substituted layer). Moreover, annealing with the 500 °C low-temperature intermediary step only provides comparable Faraday rotation without any significant improvement. It is possible that the smaller Faraday rotations in YIG/CeYIG/YIG is due to the positive Faraday rotation contribution of +500 °/cm from YIG, which counteracts the accumulated rotation from CeYIG. On the other hand, in seedlayer-free CeTbIG a Faraday rotation of −3550 °/cm is obtained with the longer anneal of 5 minutes, which is better than the Faraday rotation of CeTbIG after annealing at 900 °C for 3 minutes and much larger than other low temperature annealing processes. Large Faraday rotations in CeTbIG are beneficial to integrated photonics because the garnet does not need a seedlayer and consequently, the interaction between the propagating mode and the cladding improves, resulting in small device footprints. The thermal processes required to exfoliate CeTbIG as nanosheets ensure high crystallinity and result in a Faraday rotation of −3200 °/cm, comparable to the films on silicon substrates. Comparison of all the data in Fig. 5 reveals a trend that shows garnets annealed at higher temperatures tend to have large Faraday rotations compared to garnets annealed at lower temperatures [7,14,17,20,21,29–33]. Correspondingly, better crystallinity is also observed at higher temperatures of annealing. While it is possible to suggest that smaller Faraday rotation from less detrimental annealing processes is optimal, this work shows that better crystallinity and large Faraday rotations need higher temperature processes, and at the same time the maximum temperature experienced by the device wafer can be restricted to room-temperature by transfer printing exfoliated films, which retain the desirable magneto-optical and crystalline properties.

Optical Materials EXPRESS

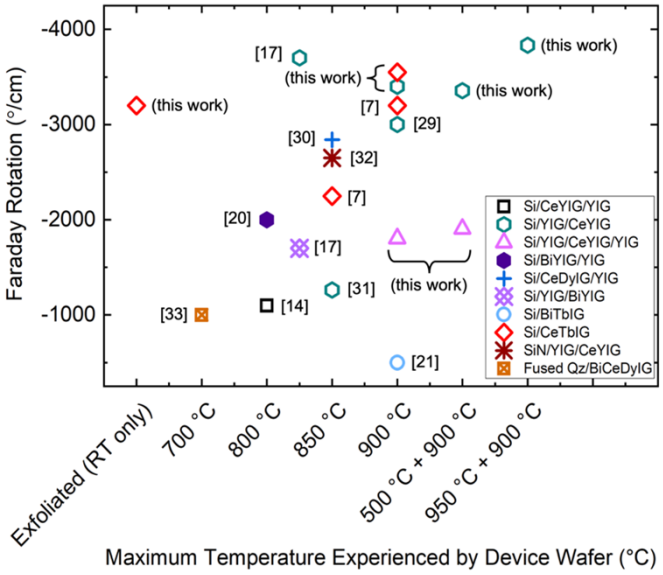

Fig. 5. The Faraday rotations for different garnets are presented against the maximum annealing temperature for the garnet in the thermal process, or impact to the thermal budget of the device wafer reported in this work and select examples from literature. Exfoliated garnets are transferred to device wafers without heating.

3. Conclusion

Enhancing the Faraday rotation is necessary in reducing the footprint of an isolator, while keeping the thermal budgets low. Quantification of crystallinity using EBSD at resolutions that match the device dimensions is necessary to identify annealing pathways to achieve desired phase crystallinity and better magneto-optical properties. In the case of CeYIG, a dual-temperature annealing process with a higher temperature spike at 950 °C for 90 s followed by 900 °C for 4 min is required to overcome the nanocrystalline phase. Faraday rotations > −3800 °/cm are achieved in a fully crystalline Si/YIG/CeYIG film stack with a one-step annealing process. On the other hand, CeTbIG films do not require a seedlayer and fully crystalline films are possible with a longer anneal at 900 °C for 5 min, where the crystallite size is between 2-4 µm and Faraday rotation greater than −3550 °/cm are obtained. Evaluation of crystallite size and the nucleation/growth of garnet crystallites on Si waveguides shows that better crystallinity is possible in wider waveguides for CeYIG claddings, while CeTbIG does not have such a dependence. This is because the nucleation sites of CeTbIG crystallites lie on the neighboring oxide regions to the waveguide, whereas the nucleation sites are on the Si waveguide for CeYIG. While large Faraday rotations and fully crystalline garnet films are possible from annealing processes at higher temperatures and longer durations, the thermal budget of garnet integration remains high. EBSD on exfoliated CeTbIG (without a substrate) shows that garnet nanosheets are fully crystalline and have large a Faraday rotation of −3200 °/cm, paving the way for low thermal budget integration.

4. Methods

Sample Growth: All garnet films in this work were sputter deposited using RF magnetron sputtering on pre-cleaned silicon substrates or silicon waveguides patterned on silicon-on-insulator (SOI) wafers. YIG seedlayers were sputtered from an oxide target of $Y_3Fe_5O_{12}$, CeYIG thin films were co-sputtered from targets of metallic Ce and composite Y_3Fe_5 and CeTbIG thin

Optical Materials EXPRESS

films were co-sputtered from metallic targets of Ce, Tb and Fe. The thin films were reactively sputtered in a 10:1 argon to oxygen ambient with a base pressure better than 2×10^{-3} torr.

Silicon Waveguide Fabrication: The Si waveguide was fabricated using SOI wafers (220 nm thick top Si and 3 μm buried oxide layer on Si substrate). The waveguide structure was patterned using electron-beam lithography (JEOL-JBX6300FS) with an E-beam resist ZEP520A as the mask and then etched using the ICP-chlorine etcher (Oxford PlasmaLab 100) with a mixture of Cl_2 and BCl_3 gases. After etching, E-beam resist was removed using NMP (N-Methyl-2-pyrrolidone) to obtain a clean surface. Another layer of E-beam resist was spin-coated to create windows for garnet deposition on the waveguides. After sputter-deposition of the garnet, the resist was lift-off using NMP and the wafer was annealed to crystallize the garnet.

Rapid Thermal Annealing (RTA): The as-deposited amorphous thin films were annealed in a Modular Process Technology RTP for 600 s in 10 sccm of O_2. The films were flushed with inert N_2 during the temperature ramp down periods. The different temperature profiles used for different garnets are provided in the main text.

Structural and Elemental Characterization: The thickness of the films was measured using a KLA Tencor P-17 surface profilometer. The X-ray diffraction patterns were recorded on a Bruker D8 Discover 2D diffractometer from a $\theta - 2\theta$ scan, which has a Co (kα) source of wavelength 1.79 Å. The polycrystalline peaks were identified using a database reference (PDF #01-071-0697) in MDI JADE. Background noise was not subtracted from the XRD measurements, which produces a slanted base-signal across all measurements. Further details of the crystal structure can be obtained from the Fachinformationszentrum Karlsruhe, D-76344 Eggenstein-Leopoldshafen (Germany), on quoting the Coll.Code 9233 for the ICSD database. Elemental composition was determined using an Oxford Instruments Electron Dispersive X-ray Spectroscopy (EDS) detector in a JEOL 6500F (field emission gun) scanning electron microscope (SEM). EBSD imaging was also carried out using the JEOL 6500F. The specimen holder was tilted to 70° at a working distance of 25 mm, with the electron beam set to an accelerating voltage of 20 kV. The single crystal silicon background was acquired prior to imaging the garnet and subtracted from the diffraction pattern. Phase identification and orientation mapping was performed using the Aztec analytical software. The specimens for EBSD imaging were not coated with a conductive layer. Crystallinity was calculated by processing the EBSD IPF images in ImageJ.

Magneto-Optical Measurements: Faraday rotation was measured using a custom-built benchtop transmission setup (shown in Fig. S4), where the planar garnet thin film sample was mounted between two electromagnets and the change in polarization was analyzed using a polarization beam splitting cube and a pair of balanced photodetectors. A maximum magnetic field of 2500 Oe was applied out-of-plane to the film surface and parallel to the light propagation. The measured rotation in degrees is divided by the thickness of the film to obtain Faraday rotation in °/cm.

Funding. Division of Electrical, Communications and Cyber Systems (2130207, 2025124); Division of Materials Research (2011401).

Acknowledgements. This work was carried out with support from the Division of Electrical, Communications and Cyber Systems in the National Science Foundation under award number ECCS-2130207. Parts of this work were carried out in the Characterization Facility and the Minnesota Nano Center, University of Minnesota, which receives partial support from the NSF through the MRSEC (Award Number DMR-2011401), and the National Nanotechnology Coordinated Infrastructure (NNCI) program under Award Number ECCS-2025124. K.S. would also like to acknowledge the support of Dr. Jason Myers for help with STEM measurements.

Disclosures. The authors declare no conflicts of interest.

Data availability. Data underlying the results presented in this paper are not publicly available at this time but may be obtained from the authors upon reasonable request.

Supplemental document. See Supplement 1 for supporting content.

Optical Materials EXPRESS

References

1. K. Srinivasan and B. J. H. Stadler, "Review of integrated magneto-optical isolators with rare-earth iron garnets for polarization diverse and magnet-free isolation in silicon photonics [Invited]," Opt. Mater. Express **12**(2), 697–716 (2022).
2. D. Jalas, A. Petrov, M. Eich, W. Freude, S. Fan, Z. Yu, R. Baets, M. Popović, A. Melloni, J. D. Joannopoulos, M. Vanwolleghem, C. R. Doerr, and H. Renner, "What is — and what is not — an optical isolator," Nat. Photonics **7**(8), 579–582 (2013).
3. D. Dai, J. Bauters, and J. E. Bowers, *Passive Technologies for Future Large-Scale Photonic Integrated Circuits on Silicon: Polarization Handling, Light Non-Reciprocity and Loss Reduction*, No. MARCH (Nature Publishing Group, 2012), Vol. 1.
4. R. Wolfe, J. Hegarty, J. F. Dillon, L. C. Luther, G. K. Celler, L. E. Trimble, and C. S. Dorsey, "Thin-film waveguide magneto-optic isolator," Appl. Phys. Lett. **46**(9), 817–819 (1985).
5. B. J. H. Stadler and T. Mizumoto, "Integrated magneto-optical materials and isolators: a review," IEEE Photonics J. **6**(1), 1–15 (2014).
6. C. Zhang, P. Dulal, B. J. H. Stadler, and D. C. Hutchings, "Monolithically-integrated TE-mode 1D silicon-on-insulator isolators using seedlayer-free garnet," Sci. Rep. **7**(1), 1–8 (2017).
7. K. Srinivasan, C. Zhang, P. Dulal, C. Radu, T. E. Gage, D. C. Hutchings, and B. J. H. Stadler, "High-Gyrotropy Seedlayer-Free Ce:TbIG for Monolithic Laser-Matched SOI Optical Isolators," ACS Photonics **6**(10), 2455–2461 (2019).
8. H. Yokoi, T. Mizumoto, T. Takano, and N. Shinjo, "Demonstration of an optical isolator by use of a nonreciprocal phase shift," Appl. Opt. **38**(36), 7409 (1999).
9. J. Fujita, M. Levy, R. M. O. Jr, L. Wilkens, and H. Dötsch, "Waveguide optical isolator based on Mach–Zehnder interferometer," Appl. Phys. Lett. **76**(16), 2158–2160 (2000).
10. D. C. Hutchings, B. M. Holmes, C. Zhang, P. Dulal, A. D. Block, S.-Y. Sung, N. C. A. Seaton, and B. J. H. Stadler, "Quasi-phase-matched Faraday rotation in semiconductor waveguides with a magnetooptic cladding for monolithically integrated optical isolators," IEEE Photonics J. **5**(6), 6602512 (2013).
11. S. Ghosh, S. Keyvaninia, Y. Shirato, T. Mizumoto, G. Roelkens, and R. Baets, "Optical isolator for TE polarized light realized by adhesive bonding of Ce:YIG on silicon-on-insulator waveguide circuits," IEEE Photonics J. **5**(3), 6601108 (2013).
12. D. Huang, P. Pintus, and J. E. Bowers, "Towards heterogeneous integration of optical isolators and circulators with lasers on silicon [Invited]," Opt. Mater. Express **8**(9), 2471 (2018).
13. K. Srinivasan and B. J. H. Stadler, "Magneto-optical materials and designs for integrated TE- and TM-mode planar waveguide isolators: a review [Invited]," Opt. Mater. Express **8**(11), 3307 (2018).
14. X. Y. Sun, Q. Du, T. Goto, M. C. Onbasli, D. H. Kim, N. M. Aimon, J. Hu, and C. A. Ross, "Single-step deposition of cerium-substituted yttrium iron garnet for monolithic on-chip optical isolation," ACS Photonics **2**(7), 856–863 (2015).
15. P. Pintus, D. Huang, P. A. Morton, Y. Shoji, T. Mizumoto, and J. E. Bowers, "Broadband TE optical isolators and circulators in silicon photonics through Ce:YIG Bonding," J. Lightwave Technol. **37**(5), 1463–1473 (2019).
16. T. Goto, M. C. Onbasli, and C. A. Ross, "Magneto-optical properties of cerium substituted yttrium iron garnet films with reduced thermal budget for monolithic photonic integrated circuits," Opt. Express **20**(27), 28507 (2012).
17. A. D. Block, P. Dulal, B. J. H. Stadler, and N. C. A. Seaton, "Growth parameters of fully crystallized YIG, Bi:YIG, and Ce:YIG films with high Faraday rotations," IEEE Photonics J. **6**(1), 1–8 (2014).
18. Y. Kim, D. J. Bang, Y. Kim, and K. H. Kim, "Magneto-optical properties of spin-coated bismuth-substituted yttrium iron garnet films on silicon substrates at 1550-nm wavelength," AIP Adv. **10**(2), 025306 (2020).
19. K. Srinivasan, A. Schwarz, J. C. Myers, N. C. A. Seaton, and B. J. H. Stadler, "Diffusion-driven exfoliation of magneto-optical garnet nanosheets: implications for low thermal budget integration in Si photonics," ACS Appl. Nano Mater. **4**(11), 11888–11894 (2021).
20. T. Fakhrul, S. Tazlaru, L. Beran, Y. Zhang, M. Veis, and C. A. Ross, "Magneto-optical Bi:YIG films with high figure of merit for nonreciprocal photonics," Adv. Opt. Mater. **7**(13), 1900056 (2019).
21. P. Dulal, A. D. Block, T. E. Gage, H. A. Haldren, S.-Y. Sung, D. C. Hutchings, and B. J. H. Stadler, "Optimized magneto-optical isolator designs inspired by seedlayer-free terbium iron garnets with opposite chirality," ACS Photonics **3**(10), 1818–1825 (2016).
22. J. L. Murray and A. J. McAlister, "The Al-Si (Aluminum-Silicon) system," Bull. Alloy Phase Diagrams **5**(1), 74–84 (1984).
23. R. W. Olesinski and G. J. Abbaschian, "The Cu−Si (copper-silicon) system," Bull. Alloy Phase Diagrams **7**(2), 170–178 (1986).
24. R. D. Jeffery, R. Sharda, R. C. Woodward, L. Faraone, and M. Martyniuk, "Crystallization of bismuth iron garnet thin films using capacitively coupled oxygen plasmas," J. Appl. Phys. **127**(4), 043302 (2020).
25. L. Jin, K. Jia, Y. He, G. Wang, Z. Zhong, and H. Zhang, "Pulsed laser deposition grown yttrium-iron-garnet thin films: Effect of composition and iron ion valences on microstructure and magnetic properties," Appl. Surf. Sci. **483**, 947–952 (2019).
26. Q. Guo, H. Zheng, L. Zheng, P. Zheng, and Q. Wu, "Target grain size dependence of the morphology, crystallinity and magnetic properties of yttrium iron garnet films," Ceram. Int. **45**(3), 3414–3418 (2019).

Optical Materials EXPRESS

27. T. E. Gage, P. Dulal, P. A. Solheid, D. J. Flannigan, and B. J. H. Stadler, "Si-integrated ultrathin films of phase-pure $Y_3Fe_5O_{12}$ (YIG) via novel two-step rapid thermal anneal," Mater. Res. Lett. **5**(6), 379–385 (2017).
28. K. Srinivasan, C. Radu, D. Bilardello, P. Solheid, and B. J. H. Stadler, "Interfacial and bulk magnetic properties of stoichiometric cerium doped terbium iron garnet polycrystalline thin films," Adv. Funct. Mater. **30**(15), 2000409 (2020).
29. Y. Zhang, Q. Du, C. Wang, T. Fakhrul, S. Liu, L. Deng, D. Huang, P. Pintus, J. Bowers, C. A. Ross, J. Hu, and L. Bi, "Monolithic integration of broadband optical isolators for polarization-diverse silicon photonics," Optica **6**(4), 473 (2019).
30. Y. Zhang, Q. Du, C. Wang, W. Yan, L. Deng, J. Hu, C. A. Ross, and L. Bi, "Dysprosium substituted Ce:YIG thin films with perpendicular magnetic anisotropy for silicon integrated optical isolator applications," APL Mater. **7**(8), 081119 (2019).
31. L. Bi, J. Hu, P. Jiang, D. H. Kim, G. F. Dionne, L. C. Kimerling, and C. A. Ross, "On-chip optical isolation in monolithically integrated non-reciprocal optical resonators," Nat. Photonics **5**(12), 758–762 (2011).
32. M. C. Onbasli, T. Goto, X. Sun, N. Huynh, and C. A. Ross, "Integration of bulk-quality thin film magneto-optical cerium-doped yttrium iron garnet on silicon nitride photonic substrates," Opt. Express **22**(21), 25183 (2014).
33. N. Radha Krishnan, R. D. Jeffery, M. Martyniuk, R. C. Woodward, M. Saunders, J. M. Dell, and L. Faraone, "Preparation and characterization of cerium substituted bismuth dysprosium iron garnets for magneto-optic applications," IEEE Trans. Magn. **52**(7), 1–4 (2016).